Article

Nb$_2$S$_4$(CS$_2$NH$_2$)$_4$—A New Precursor for NbS$_2$ and Its Transition Metal Inserted Derivatives

Sebastian Mangelsen *[ID], Patrick Zimmer, Christian Näther and Wolfgang Bensch [ID]

Institute of Inorganic Chemistry, Kiel University, Max-Eyth Straße 2, D-24118 Kiel, Germany
* Correspondence: smangelsen@ac.uni-kiel.de

Abstract: Transition metal inserted NbS$_2$ (T$_x$NbS$_2$) compounds receive great attention due to their intriguing and diverse magnetic and electric transport properties. Typically, these compounds are prepared by high-temperature synthesis from the elements, which is time and energy-consuming and yields highly crystalline products. So far, no route for preparing these compounds from precursors by thermal decomposition has been reported. Herein, we report the synthesis of a dithiocarbamate of niobium Nb$_2$S$_4$(CS$_2$NH$_2$)$_4$ as a precursor for the synthesis of NbS$_2$ by this preparative strategy. Furthermore, we demonstrate that a co-decomposition with dithiocarbamates of transition metals (here, Co and Pd) is a viable route for the synthesis of T$_x$NbS$_2$-type compounds. This is a promising route for the exploration of these compounds' properties in the form of, e.g., nanocrystalline or thin film samples.

Keywords: transition metal dichalcogenides; dithiocarbamates; thermal decomposition; precursor

1. Introduction

Transition metal dichalcogenides (TMDCs) with the general formula MQ$_2$ (M = Ti, Zr, Hf, Nb, Ta, Mo, W; Q = S, Se, Te) crystallize in a layered structure, in which the transition metal cation is either in an octahedral or trigonal prismatic environment of chalcogenide ions [1,2]. The layers are stacked onto each other, and depending on the transition metal and the chalcogen, the layers are separated by a van der Waals gap. For a couple of years, TMDCs have been the focus of research after the discovery of a large variety of unusual physical properties like non-saturating magnetoresistance (e.g., WTe$_2$ [3,4], MoTe$_2$ [5,6], HfTe$_2$ [7,8]), Dirac or Weyl semimetal properties (e.g., WTe$_2$ [9,10], NiTe$_2$ [11], MoTe$_2$ [12,13]), superconductivity [14–17] and more. Sophisticated synthetic routes for tuning the chemical and physical properties of TMDCs are intercalation or insertion of guest species into the van der Waals gaps, thus generating a host–guest complex [18,19]. The effect of intercalation or insertion leaves the structure of the host intact but alters the chemical and physical properties.

More than half a century ago, the insertion of the 3d metals Mn, Fe, Co, and Ni in the van der Waals gap of the layered compounds NbS$_2$ and TaS$_2$ was reported [20]. Since then, significant progress in this field has been made, as insertion with other metals has been achieved and other hosts like TiS$_2$ [21,22], (Nb,Ta)Se$_2$ [23] and (Zr,Hf)S$_2$ [24,25] were identified. Those compounds are of particular interest due to their diverse magnetic and electric properties [20,26–28]. These properties can be tuned, typically within a reasonable range, due to the phase width that those compounds show with respect to the amount of inserted transition metal [27,29,30]. The majority of studies were performed on single crystal specimens and only a few reports on devices fabricated via micromechanical exfoliation exist [31–33].

An attractive route for bottom-up synthesis of nanoscaled materials is the use of precursor compounds. In the case of (Mo,W)S$_2$, the tetrathiosalts (NH$_4$)$_2$MS$_4$ are suitable compounds and allow for further chemical modification by cation exchange, e.g., with

3d-metal complexes [34–36]. Similar compounds are not known for Nb and Ta; however, for the former, some dithiocarbamate complexes exist [37]. Dithiocarbamate complexes are well known to be suitable precursors for the preparation of sulfides [38,39], and corresponding complexes containing, for example, Co or Ni, are straightforward to synthesize. For known Nb dithiocarbamate complexes of the general formula $[Nb_2S_4(CS_2NR_2)_4]$ (R = organic substituent, typically alkyl chain), the $[Nb_2S_4]^{4+}$-cation is the central ion surrounded by the dithiocarbamate ligands. Yet the unsubstituted compound with R = H was not reported, although its thermal decomposition should yield pure NbS_2 virtually free of impurities from the ligand. Precursors containing carbon-rich ions or ligands tend to form metal sulfides with significant carbon content, as exemplified by $(NR_4)_2MS_4$ [40,41]. For thioxanthate complexes of Nb with the general formula $[Nb_2S_4(CS_2CR_2)_4]$ the formation of amorphous carbon containing NbS_2 was reported to occur upon thermal decomposition at 500 °C [42]. Therefore, the known plethora of compounds bearing the $[Nb_2S_4]^{4+}$-cation, along with other carbon or oxygen-containing ligands, appear less appealing as precursors for the preparation of pure NbS_2.

Thus, a rationally designed route for 3d-metal inserted NbS_2 would be the co-decomposition of $[Nb_2S_4(CS_2NH_2)_4]$ (**1**) and $T^{n+}(CS_2NH_2)_n$ at suitable temperatures. Herein, we demonstrate the feasibility of this route. The synthesis and characterization of the novel compound $[Nb_2S_4(CS_2NH_2)_4]$ are described, as well as the synthesis of T_xNbS_2 by the codecomposition route.

2. Results and Discussion

2.1. Synthesis

According to procedures described in the literature, dithiocarbamates containing the $[Nb_2S_4]^{4+}$ cation can be prepared by treatment of $(Et_4N)_4Nb_2S_4(SCN)_8$ with salts of the desired ligand in water or in the two-phase system water/CH_2Cl_2 [37]. Following both approaches, we were not able to obtain the title compound when reacting $(Et_4N)_4Nb_2S_4(SCN)_8$ with $NH_4CS_2NH_2$. The IR spectra of the solid products still showed strong bands of the NCS^-ligand. Instead, the aqueous solution containing $[Nb_2S_4(SCN)_8]^{4-}$-anions (obtained after extraction of the product of fusing NbS_2Cl_2 with KSCN with water) was reacted directly with a solution of $NH_4CS_2NH_2$. The reaction appears to be fast as a copious precipitate forms immediately after mixing both solutions, and the solution turns from orange to colorless. But, this product is not the title compound as evidenced by IR spectra, elemental analysis, and X-ray powder diffraction (see Figures S1 and S2 and accompanying discussion). Instead, a prolonged treatment (~20 h) with the ligand is required to ensure complete exchange of the ligands.

Initially, acetone was used to recrystallize the raw product and for single crystal growth. However, it turned out that the crystal structure (**1-Acetone**) from this batch contained four additional formula units of acetone and did not match the X-ray diffraction pattern obtained for the recrystallized powder (see Figure S3). Crystallization from further solvents proved methanol/water to be a suitable mixture for obtaining single crystals of the ansolvate **1**. One should note that in the single crystal structure, a position for an oxygen (i.e., a water molecule) with an occupancy of 0.4 was found. However, the IR spectra for the powdered samples (vide infra) indicate the absence of any solvent.

In further experiments, it was observed that **1** can be obtained phase pure from slow evaporation of a solution in acetone in a petri dish (see Figure S3). In contrast, evaporation in a rotary evaporator leads to a phase mixture of **1** and **1-Acetone**. This points to kinetic factors determining which crystalline phase grows since elevated temperature and reduced pressure should favor the ansolvate under the conditions in the rotary evaporator (Figure S4).

$Co(CS_2NH_2)_3$ is a suitable precursor for the preparation of T_xNbS_2-type compounds by co-decomposition of precursors. The crystal structure has been reported. However, after synthesis in water, a diffraction pattern different from the reported structure [43] was observed, which could not be matched with an entry in the CSD database. It was found

that this product is the monohydrate $Co(CS_2NH_2)_3 \cdot H_2O$. The crystal structure was solved and refined from XRPD data. The final difference plot is presented in Figure S5, along with selected results from the Rietveld refinement (Table S1).

For $Pd(CS_2NH_2)_2$, no crystal structure was reported in the CSD database. The product obtained by slow evaporation from acetone showed a similar diffraction pattern as $Ni(CS_2NH_2)_2$ [44]. For $Pd(CS_2NH_2)_2$, a Rietveld refinement using the structure of $Ni(CS_2NH_2)_2$ as a starting model was carried out successfully to refine the crystal structure. The difference plot, as well as selected details of the refinement, can be found in Figure S6 and Table S1. There are minor differences between the crystal structures of the two compounds regarding the relative orientation of the individual complexes.

2.2. Vibrational Spectroscopy

The vibrational spectra obtained from the powder of **1** are presented in Figure 1. As outlined in the discussion of the synthetic procedure, the solution from which **1** is prepared contains the complex anion $[Nb_2S_4(SCN)_8]^{4-}$. The absence of a band in the region of 2080 cm^{-1} (CN stretching vibration of the NCS^- ligand) provides evidence for a complete exchange of these ligands. The vibrations of the dithiocarbamate ligand can be assigned to the bands at 3399, 3274, 3144 cm^{-1} (υ N-H), 1580 cm^{-1} (NH_2 bending), 1376 cm^{-1} (C-N stretching), 840 cm^{-1} (C-S stretching), 1236 cm^{-1} and extending bands to 1050 cm^{-1} as well as 854 and 841 cm^{-1} (NH_2 rocking coupled to C-S stretching), 630 cm^{-1} (C-S stretching) [45]. The Raman spectrum shows known characteristic bands for the $[Nb_2S_4]^{4+}$ core with the S-S vibration at 565 cm^{-1} [37,42,46] and various Nb-S vibrations in the range of 370–250 cm^{-1}.
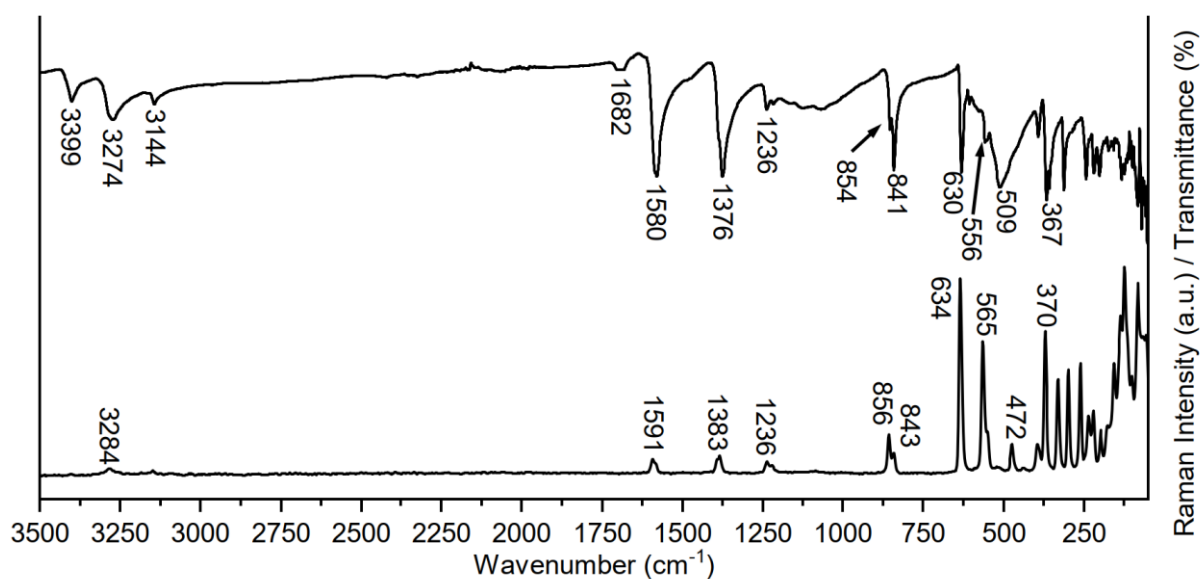
Figure 1. Infrared and Raman spectra of $Nb_2S_4(CS_2NH_2)_4$.

2.3. Crystal Structures

Compound **1** crystallizes in the orthorhombic space group *Pbcn* with Z = 4 formula units in the unit cell. The asymmetric unit consists of one crystallographically independent Nb^{4+} cation, one independent $[S_2]^{2-}$ anion, and four dithiocarbamate anions in general positions, as well as one water molecule that is located on a crystallographic mirror plane (Figure S7). The Nb cations are 8-fold coordinated by four S atoms of two dithiocarbamate anions and both S atoms of two $[S_2]^{2-}$ anions within an irregular coordination (Table S3). Each two Nb cations are linked by two μ-1,1,2,2 bridging $[S_2]^{2-}$ anions into discrete clusters that are located on centers of inversion (Figure 2). The geometric parameters of the $Nb_2S_4^{4+}$ core (Table S3) are in agreement with the literature data [37].
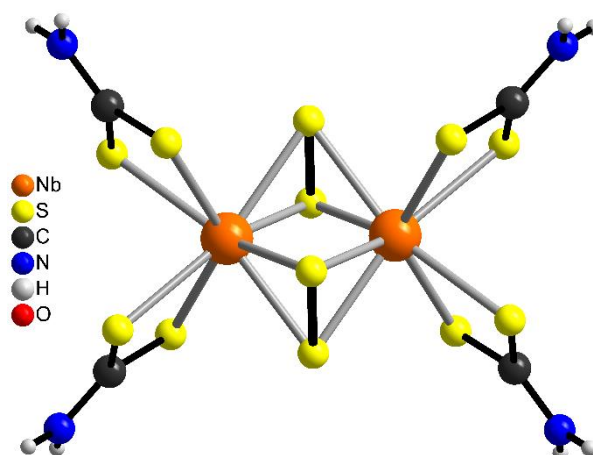
Figure 2. Excerpt of the crystal structure of compound **1** with a view of the cluster molecule.

In the crystal structure, the cluster molecules are linked by intermolecular N-H···S hydrogen bonding between the dithiocarbamate S atom and the N-H hydrogen atom of a neighboring anion into layers that are parallel to the a-b plane (Figure S8 and Table S4). Within the layers the water molecules are located and hydrogen bonded to the H atoms of the dithiocarbamate molecules. There are additional intermolecular hydrogen bonds that correspond to only weak interactions.

As mentioned in Section 2.1, the crystal structure of **1-Acetone** was also determined, the details of which are presented in the Supplemental Information (Figures S9 and S10 and Tables S5 and S6).

2.4. Thermal Decomposition

It is well known that metal dithiocarbamates are suitable precursors for the generation of metal sulfides. Many of these compounds thermally decompose at temperatures around 200–250 °C, frequently forming thiocyanates that transform into sulfides at even higher temperatures [38,39].

Measurements using differential thermoanalysis and thermogravimetry (DTA-TG) of **1** shows a first mass step of 42 wt.-% starting around 200 °C, with a maximum in the first derivative of the TG curve (DTG curve) at 260 °C (Figure 3a). This is accompanied by an endothermic event in the DTA curve with an onset temperature of ~210 °C and a peak temperature coinciding with the peak in the DTG curve. The expected mass loss for the formation of $Nb_2S_4(SCN)_4$ as intermediate by emission of H_2S would be 20 wt.-%, much lower than observed. Alternatively, the formation of NbS_3 can be expected, with a theoretical mass loss of 44.6 wt.-%, which is in good agreement with the experimental value. A second, rather sluggish mass loss of 16.1% starts around 475 °C and is not completed up to 600 °C where the measurement was terminated. The mass loss is higher than expected for the removal of one formula unit of sulfur from NbS_3. Analysis of the residual by XRPD showed the formation of a niobium oxide (Figure S11), despite the use of inert gas (Ar). Likely, very low residual amounts of oxygen or water in the inert gas are sufficient to cause oxide formation due to the oxophilicity of Nb.

In an attempt to learn more about the evolution of crystalline phases during thermal decomposition, we performed temperature-resolved XRPD in the range of 25–550 °C in an open glass capillary (see Figure 3b). Compound **1** remains crystalline and stable up to ~190 °C. Slightly above 200 °C, thermal decomposition is complete, and the intermediately formed product is amorphous. At 475 °C, one reflection appears, which is assigned to the same oxide phase observed after the DTA-TG experiment.
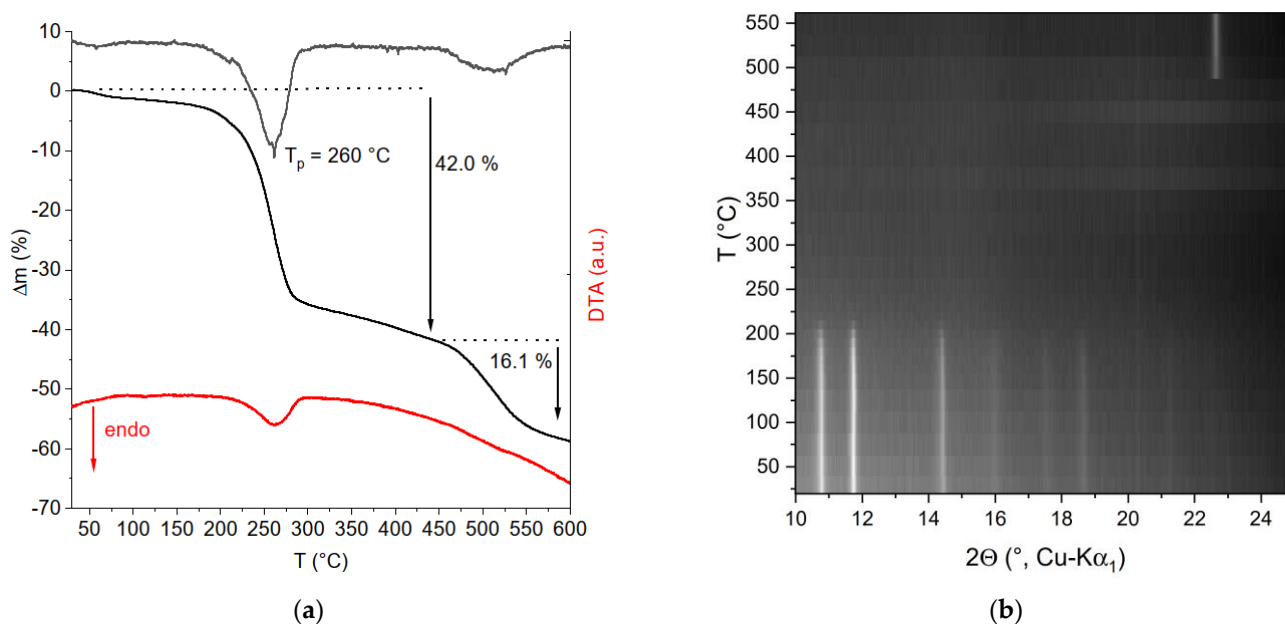
Figure 3. (**a**) DTA-TG curve for **1** in the range of 30–600 °C. Additionally, the DTG curve is shown (top trace). (**b**) Temperature resolved XRPD data of **1**. Above 200 °C, the sample is amorphous, and from ~475 °C, crystalline $Nb_{16.8}O_{42}$ [47] can be observed.

In order to test the use of **1** as a precursor for NbS_2 in the absence of oxygen or moisture, a small amount (drop casted on a Si/SiO$_2$ substrate) was decomposed in a sealed quartz ampoule at 1000 °C for 1 h. On the substrate, the NbS_2 grows with a strongly preferred orientation such that the layers grow preferentially parallel to the substrate's surface (see Figure S12 and accompanying explanation). The XRPD pattern of the resulting black powder that was scratched off the substrate is shown in Figure 4a. The sample consists mainly of 3R-NbS_2 with small amounts of 2H-NbS_2. The width of the diffraction lines is virtually only limited by instrumental resolution, i.e., there is no significant domain size or strain contribution. Furthermore, no signs of stacking faults (i.e., broadening of cross reflections) are evident, unlike typical synthesis of NbS_2 by means of preparation from the elements at temperatures of 900–1000 °C [14,48–50]. The lattice parameters for 3R-NbS_2 were determined via a Pawley fit to be *a* = 3.334(1) Å and *c* = 17.844(1) Å, which indicates non-stoichiometric $Nb_{1+x}S_2$ according to the study of Fischer et al., not surprising for a decomposition in a vacuum [50]. In a first attempt towards the synthesis of transition metal inserted NbS_2, the same approach was used for a precursor mixture of **1** and $Co(CS_2NH_2)_3$ with a targeted composition of $Co_{1/3}NbS_2$. The XRPD pattern in Figure 4b shows that the target compound was obtained, and the sharp reflections indicate an excellent crystallinity of the sample.

After this first test, a more extended series of decomposition experiments was performed in sealed quartz tubes with quantities of ~30 mg powdered precursor. Both pure **1** as well as a co-decomposition with $Pd(CS_2NH_2)_2$ was tested. The latter was chosen since little has been reported experimentally on the system Pd_xNbS_2 [51], whereas Ag_xNbS_2 [52,53] is well known. First, we shall discuss the product evolution of decomposing pure **1** at different temperatures, and the XRPD patterns are shown in Figure 5a. A temperature of 300 °C yields an amorphous product, in line with the results from the in situ experiment (see Figure 3b). There is one broad halo located around 15° 2Θ, which could indicate some short-range order similar to amorphous WS_3 [54]. After decomposition at 700 °C, the product shows broad reflections indicating domain sizes on the nanoscale. No clear assignment to either of the two known polytypes (2H and 3R type) of NbS_2 can be made. The broadening of the cross-plane reflections (cf. the observed and calculated reflections around 38 and 48° 2Θ) is most pronounced, indicating the presence of severe stacking faults. The product obtained at 1000 °C shows overall sharper reflections, indicating the

growth of the crystallites. Furthermore, some very sharp reflections can be observed, which can be assigned to unfaulted $3R\text{-}NbS_2$. The crystallinity for this part of the sample is similar to that seen in the data in Figure 4. The origin of this effect is not clear. Possibly, this is related to the exact area where the precursor was decomposed, i.e., at the wall of the ampoule or in the volume of the precursor. The precursor being dispersed on a surface vs. being in a compact volume may play a role here.
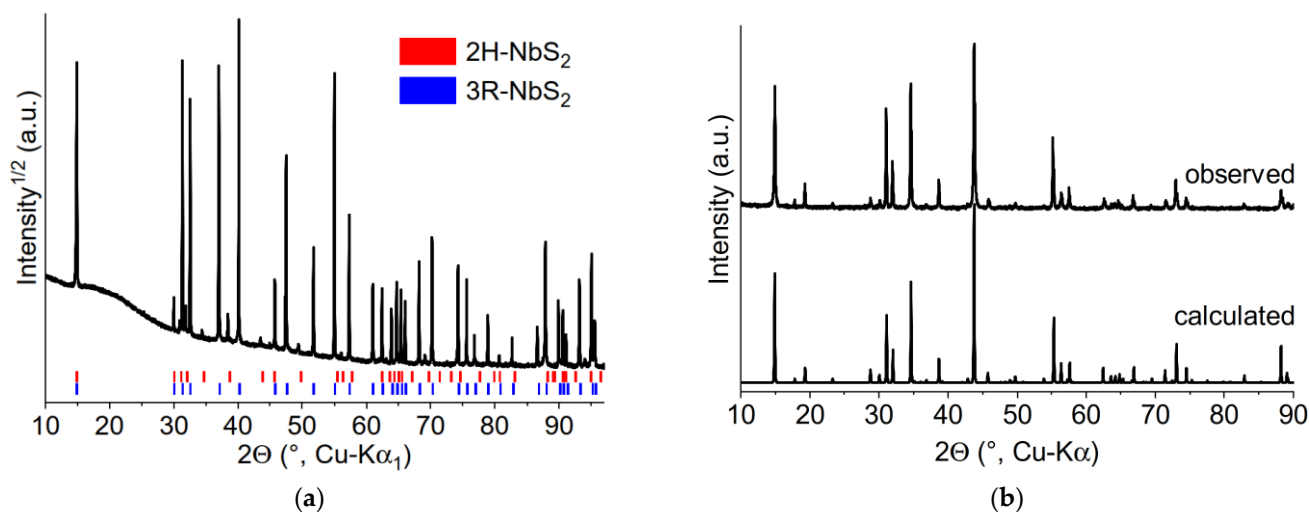
Figure 4. (**a**) XRPD pattern of the product of the decomposition of **1** at 1000 °C deposited on a Si/SiO_2 substrate. The tick marks for 2H- and $3R\text{-}NbS_2$ indicate the latter as the main phase, aside from a small amount of $2H\text{-}NbS_2$. (**b**) Comparison of the calculated ($Co_{1/3}NbS_2$) and observed XRPD pattern of the product obtained by co-decomposition of **1** and $Co(CS_2NH_2)_3$ by the same approach.
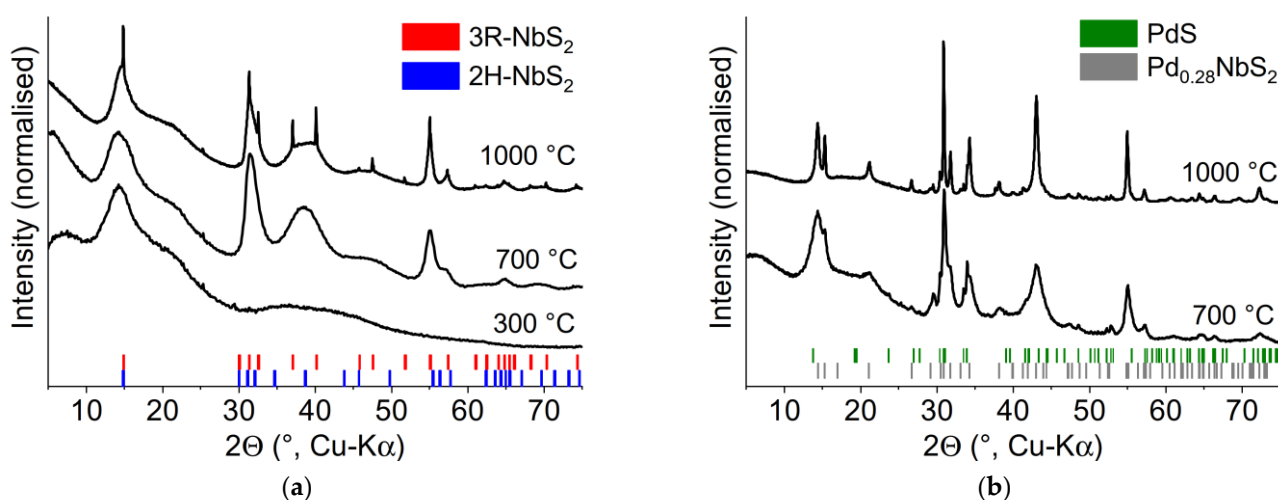
Figure 5. (**a**) XRPD pattern of the decomposition products of 30 mg of **1** in a sealed quartz ampoule at temperatures as indicated. (**b**) XRPD pattern of the decomposition products after co-decomposition of **1** and $Pd(CS_2NH_2)_2$. Vertical bars indicate the positions of Bragg reflections.

In Figure 5b, the XRPD pattern of the products of the co-decompositions are shown. Again, the product obtained after decomposition at 1000 °C shows the sharpest reflections, and two phases can be identified: A Pd inserted NbS_2 and minor impurities of PdS (3.5 wt.-%, vide infra). Two additional weak reflections remained unexplained (see Figure S13). For the Pd_xNbS_2, the best fit could be obtained with a structural model using the $2a \times 2a$ type superstructure, well known for other transition metal inserted TMDCs [55]. For this type of superstructure, the Pd^{2+}-cations are ordered in the interlayer space at a distance of two times the lattice parameter a of the host structure $2H\text{-}NbS_2$. This differs from

the disordered arrangement reported previously for $Pd_{0.23}NbS_2$ [51] and may be related to a higher content of Pd. A detailed refinement proved the suitability of this structure model. The content of Pd was estimated using a Rietveld refinement to be $Pd_{0.28}NbS_2$, deviating only slightly from the ideal value of 0.25 for this superstructure type. The Pd was found to be slightly disordered in the interlayer space, with some of the Pd^{2+}-cations residing on the second available Wyckoff position in the interlayer space (see Figure S14 for a depiction of the crystal structure). The lattice parameter c is larger compared to $Pd_{0.23}NbS_2$ (12.2298(8) Å vs. 12.2147(18) Å [51]), further evidencing a larger Pd-content compared to this compound. The difference plot of the refinement and details of the crystal structure can be found in Figure S13 and Tables S7 and S8. From the quantification, the ratio of Pd:Nb in the sample was calculated to be ~1:3 in agreement with the weighed precursor mixture. The formation of PdS as a side phase may either indicate an incomplete reaction or a solubility limit of Pd in Pd_xNbS_2.

These results show the suitability of **1** as a precursor for NbS_2 as well as the feasibility of synthesizing transition metal inserted NbS_2 via a facile co-decomposition route. However, there are aspects that may be addressed in future work. First, the synthesis of **1** from NbS_2Cl_2 as starting material has an overall yield of ~25% (for $Nb_2S_4(CS_2NEt_2)_4$ 33% were reported), which leaves room for improvement. Theoretically, **1** may be obtained from NbS_2Cl_2 by exchange of the chloride anion by $[CS_2NH_2]^-$ -anions since the former contains the $[Nb_2S_4]^{4+}$ cation in the crystal structure [37,56]. The step of melting this compound in KSCN is accompanied by significant losses in the yield [37]. If the major barrier for activating NbS_2Cl_2 for substitution of the chloride might be the reaction in an ionic medium, then ionic liquids or deep eutectic solvents may be a future perspective for enhancing the yield.

Furthermore, the results show that **1** is suitable for synthesizing NbS_2 after a short thermal treatment. It will be interesting to see how different atmospheres (e.g., flow of inert gas) will affect the microstructure of the samples. Also, the observed differences in crystallinity for the different decomposition experiments call for clarification. The results so far suggest that dispersion of the precursor on a surface favors the formation of a highly crystalline product. Hence, the directed decomposition on different substrates may affect crystallinity and may induce the preferred orientation of the crystallites. This is suggested by the decomposition experiment we carried out on the Si/SiO_2 substrate that led to crystallization with a pronounced preferred orientation.

So far, we have explored temperatures as low as 700 °C for the co-decomposition. The TG-data of **1** (see Figure 3) suggests that even lower decomposition temperatures are possible. However, a more pronounced line broadening in the XRPD patterns is expected and might obscure the relatively weak superstructure reflections that characterize the insertion compounds. This question may then be answered with transmission electron microscopy and spatially resolved EDX and is left open for future work.

A major achievement of this work is the development of the co-decomposition route for the synthesis of transition metal inserted NbS_2. Given these compounds' chemical and compositional variability, this holds great potential when exploring their physical properties and applying this route to synthesize them as nanomaterials or films. The latter may be obtained when depositing mixed precursor solutions on suitable substrates with subsequent thermal treatment.

For Pd_xNbS_2, we reported for the first time the formation of an ordered superstructure in the interlayer space. As this type of compound is only scarcely investigated, we suggest further studies on its structural properties (i.e., formation of superstructures and solubility limit of Pd) as well as its physical properties.

3. Materials and Methods

3.1. Preparations

$NH_4CS_2NH_2$ was prepared according to the procedure described by Teske and Bensch [57].

NbS$_2$Cl$_2$: The procedure was adopted from the literature [58,59]. Nb (1.224 g, 13.2 mmol, chempur, 99.9%), NbCl$_5$ (2.371 g, 8.8 mmol Alfa Aesar, 99.9%) and S (1.409 g, 44 mmol chempur, 99.999%) were ground and loaded in a quartz ampoule in a glove box (Ar, p_{O2} <1 ppm, p_{H2O} < 1 ppm) as NbCl$_5$ hydrolyses in humid air. The ampoule was evacuated to $p < 3 \times 10^{-4}$ mbar and sealed. The charge was heated to 500 °C, held there for 2 days, and cooled to room temperature. The raw product was transferred into an ampoule of 16 mm inner diameter, and chemical vapor transport was carried out in a temperature gradient of 500 °C → 400 °C. On the cold end side phase, pure NbS$_2$Cl$_2$ was obtained in the form of deep red crystals. The powder is of orange color.

Nb$_2$S$_4$(CS$_2$NH$_2$)$_4$: This preparation is a variation of the procedure given by Sokolov et al., [37] NbS$_2$Cl$_2$ (0.5 g, 2.2 mmol)) was ground with KSCN (5.0 g, 51 mmol, dried at 160 °C) and loaded in a quartz ampoule with an inner diameter of 16 mm. After evacuation to $p < 3 \times 10^{-4}$ mbar, it was sealed and heated for 48 h to 180 °C. The reddish melt was well-ground and extracted with demineralized water (~15 mL). An orange solution was obtained after filtration, to which a solution of freshly prepared NH$_4$CS$_2$NH$_2$ (0.727 g, 6.6 mmol) in demineralized water was added. Within seconds, a copious orange precipitate had formed, but stirring was continued for 20 h in order to complete the reaction. The orange precipitate was filtered off and washed with water. The raw product was recrystallized from acetone. Yield: ~25% based on NbS$_2$Cl$_2$. Elemental analysis: C 6.95 (calcd. 7.04); H 1.49 (calcd. 1.18); N 8.02 (calcd. 8.21); S 56.40 (calcd. 56.36).

Co(CS$_2$NH$_2$)$_3$: CoCl$_2$·6H$_2$O (180 mg, 756 µmol) and NH$_4$CS$_2$NH$_2$ (250 mg, 2.3 mmol) were dissolved in demineralized water each. After mixing the solution, a dark green solution formed, and instantaneously, a green precipitate formed. Stirring was continued for 2 h, after which the product was recovered by filtration and washing with demineralized water. The diffraction pattern of the raw product does not match the pattern known in the literature for Co(CS$_2$NH$_2$)$_3$ [43]. Thus, the product was recrystallized from acetone, after which the proper phase was obtained. Yield: ~80%. Elemental analysis: C 12.21 (calcd. 10.19); H 2.15 (calcd. 2.28); N 12.46 (calcd. 11.89); S 56.60 (calcd. 54.44).

Pd(CS$_2$NH$_2$)$_2$: K$_2$PdCl$_2$ (490 mg, 1.5 mmol) and NH$_4$CS$_2$NH$_2$ (364 mg, 3.3 mmol) were dissolved in demineralized water each. An orange precipitate formed quickly, which was filtered off, washed with water, and dried in vacuo. The raw product was recrystallized from acetone. Yield: ~95%. Elemental analysis: C 8.67 (calcd. 8.26); H 1.59 (calcd. 1.39); N 9.73 (calcd. 9.64); S 45.29 (calcd. 44.12).

For the co-decomposition of precursors, weighed amounts of the precursors were dissolved in acetone, and the solvent was slowly evaporated in a petri dish. The precursor mixture was collected and transferred in a quartz ampoule (inner volume ~25 cm^3), evacuated to $p \sim 1 \times 10^{-1}$ mbar, and flame-sealed. The ampoule was heated to the target temperature at a rate of 100 °C/h, held there for one hour, and slowly cooled to room temperature. The resulting black powders were stored in a glove box (Ar, $p_{O2/H2O}$ < 1 ppm).

3.2. X-ray Powder Diffraction

Data for structure solution of Co(CS$_2$NH$_2$)·H$_2$O was collected on an STOE Stadi-P diffractometer equipped with Mo-Kα_1 radiation (Johansson type Ge (111) monochromator) and a Dectris MYTHEN 1K detector in Debye-Scherrer geometry. The sample was loaded in a capillary (Spezialglas Nr. 14, Hilgenberg) of 0.7 mm diameter and spun during the measurement.

All operations for structure solution and refinement were carried out in TOPAS Academic V. 6.0 [60]. Indexing using singular value decomposition [61] of the diffraction pattern of Co(CS$_2$NH$_2$)·H$_2$O yielded a monoclinic cell with a = 7.1516 Å, b = 14.6611 Å, c = 11.7222 Å and β = 99.092° and the space group $P2_1/c$ with only one unindexed reflection. After refining the lattice parameters, zero point error, and accounting for minor microstructural effects using a Pawley fit in the next step, charge flipping was applied to solve the structure. The sites of both cobalt and sulfur atoms could clearly be identified. In the next step, these coordinates were transferred to a real-space approach for a simulated

annealing (SA) [62]. The $CS_2NH_2^-$ ligands were modeled as rigid bodies with bond lengths and angles taken from the literature [43]. The water molecule was modeled by a single oxygen atom that was allowed to translate freely during the SA run. The structure could quickly be solved, and in the final refinement, all parameters (zero point error, lattice parameters, microstructure, atomic coordinates, S-C-S angle of the dithiocarbamate, and B_{iso} values) could be refined stably. The details of the final refinement can be found in Table S1. The final difference plot is displayed in Figure S5.

The XRPD pattern of the decomposition products was measured on a Panalytical Empyrean diffractometer equipped with Cu-K$_\alpha$ radiation, a focusing X-ray mirror, and a PIXcel 1D detector in transmission geometry. The samples were kept between two sheets of Scotch® tape. The patterns of the samples obtained by decomposition on Si/SiO$_2$ wafers were measured on an STOE Stadi-P diffractometer equipped with Cu-Kα_1 radiation (Johansson type Ge (111) monochromator) and a Dectris MYTHEN 1K detector on Debye–Scherrer geometry.

The XRPD pattern of the decomposed precursor **1** on a Si/SiO$_2$ substrate was recorded on a Panalytical X'Pert Pro MPD equipped with Cu-Kα radiation, a Göbel mirror, parallel plate collimator and PIXcel 1D detector in Bragg–Brentano geometry. The sample was held on stage for flat samples.

The temperature-resolved XRPD data was collected on an STOE Stadi-P diffractometer equipped with Cu-Kα_1 radiation (Johansson type Ge (111) monochromator) and a Dectris MYTHEN 1K detector in Debye–Scherrer geometry. The samples were loaded in 0.5 mm thick quartz capillaries, heated in an STOE capillary furnace, and spun during the measurement. The temperature increments were 25 °C per step, and each measurement took ~2 h.

3.3. Single Crystal X-ray Analysis

The data collections were performed using a XtaLAB Synergy, Dualflex, HyPix diffractometer from Rigaku [63] and an Imaging Plate Diffraction System (IPDS-2) from STOE & CIE [64] with MoKα-radiation (λ = 0.71073 Å). For compound **1**, a multi-scan absorption correction was performed using CrysAlisPro Field [63] using spherical harmonics, which were implemented in the SCALE3 ABSPACK scaling algorithm. For compound **1-Acetone**, a numerical absorption correction was performed using X-Red and X-Shape as part of the program package X-Area [64]. The structures were solved with SHELXT [65] and refined using SHELXL-2016 [66] and SHELXL-2018 [66]. All atoms were refined anisotropic. The C--H and N-H H atoms were initially located in a difference map but finally positioned with idealized geometry (methyl H atoms allowed to rotate but not to tip) and refined isotropic with $U_{iso}(H) = 1.2\ U_{eq}(C,N)$ (1.5 for methyl H atoms) using a riding model. The O atom in the compound is not fully occupied. Its H atom was located in a difference map, its distance was set to ideal values, and finally it was refined isotropic with $U_{iso}(H) = 1.5\ U_{eq}(O)$ using a riding model.

CCDC 2303610 (**1**), CCDC 2303609 (**1-Acetone**), CCDC 2303611 (Co(CS$_2$NH$_2$)$_3$·H$_2$O) and CCDC 2303612 (Pd(CS$_2$NH$_2$)$_2$) contain the supplementary crystallographic data for this paper. These data can be obtained free of charge from the Cambridge Crystallographic Data Centre via http://www.ccdc.cam.ac.uk/data_request/cif.

4. Conclusions

In this work, we established the synthesis of the title compound Nb$_2$S$_4$(CS$_2$NH$_2$)$_4$. It proved to be thermally labile above 200 °C and thus is suitable as a precursor for synthesizing NbS$_2$ by thermal decomposition. Furthermore, the co-decomposition with dithiocarbamates of Co and Pd proved a viable route for the rapid synthesis of NbS$_2$ inserted with these metals. This opens up an intriguing route for synthesizing these compounds as thin films or nanomaterials and exploring their physical properties in this state of matter.

Furthermore, we observed for the first time the formation of an ordered superstructure for $Pd_{0.28}NbS_2$, which calls for a more extensive investigation of the structural and physical properties of this type of compound.

References

1. Wilson, J.A.; Yoffe, A.D. The Transition Metal Dichalcogenides Discussion and Interpretation of the Observed Optical, Electrical and Structural Properties. *Adv. Phys.* **1969**, *18*, 193–335. [CrossRef]
2. Katzke, H.; Tolédano, P.; Depmeier, W. Phase Transitions between Polytypes and Intralayer Superstructures in Transition Metal Dichalcogenides. *Phys. Rev. B* **2004**, *69*, 134111. [CrossRef]
3. Ali, M.N.; Xiong, J.; Flynn, S.; Tao, J.; Gibson, Q.D.; Schoop, L.M.; Liang, T.; Haldolaarachchige, N.; Hirschberger, M.; Ong, N.P.; et al. Large, Non-Saturating Magnetoresistance in WTe_2. *Nature* **2014**, *514*, 205–208. [CrossRef] [PubMed]
4. Luo, Y.; Li, H.; Dai, Y.M.; Miao, H.; Shi, Y.G.; Ding, H.; Taylor, A.J.; Yarotski, D.A.; Prasankumar, R.P.; Thompson, J.D. Hall Effect in the Extremely Large Magnetoresistance Semimetal WTe_2. *Appl. Phys. Lett.* **2015**, *107*, 182411. [CrossRef]
5. Chen, F.C.; Lv, H.Y.; Luo, X.; Lu, W.J.; Pei, Q.L.; Lin, G.T.; Han, Y.Y.; Zhu, X.B.; Song, W.H.; Sun, Y.P. Extremely Large Magnetoresistance in the Type-II Weyl Semimetal $MoTe_2$. *Phys. Rev. B* **2016**, *94*, 235154. [CrossRef]
6. Thirupathaiah, S.; Jha, R.; Pal, B.; Matias, J.S.; Das, P.K.; Sivakumar, P.K.; Vobornik, I.; Plumb, N.C.; Shi, M.; Ribeiro, R.A.; et al. $MoTe_2$: An Uncompensated Semimetal with Extremely Large Magnetoresistance. *Phys. Rev. B* **2017**, *95*, 241105. [CrossRef]
7. Mangelsen, S.; Naumov, P.G.; Barkalov, O.I.; Medvedev, S.A.; Schnelle, W.; Bobnar, M.; Mankovsky, S.; Polesya, S.; Näther, C.; Ebert, H.; et al. Large Nonsaturating Magnetoresistance and Pressure-Induced Phase Transition in the Layered Semimetal $HfTe_2$. *Phys. Rev. B* **2017**, *96*, 205148. [CrossRef]
8. Mangelsen, S.; Bensch, W. $HfTe_2$: Enhancing Magnetoresistance Properties by Improvement of the Crystal Growth Method. *Inorg. Chem.* **2020**, *59*, 1117–1124. [CrossRef]
9. Pletikosić, I.; Ali, M.N.; Fedorov, A.V.; Cava, R.J.; Valla, T. Electronic Structure Basis for the Extraordinary Magnetoresistance in WTe_2. *Phys. Rev. Lett.* **2014**, *113*, 216601. [CrossRef]
10. Wu, Y.; Mou, D.; Jo, N.H.; Sun, K.; Huang, L.; Bud'ko, S.L.; Canfield, P.C.; Kaminski, A. Observation of Fermi Arcs in the Type-II Weyl Semimetal Candidate WTe_2. *Phys. Rev. B* **2016**, *94*, 121113. [CrossRef]
11. Xu, C.; Li, B.; Jiao, W.; Zhou, W.; Qian, B.; Sankar, R.; Zhigadlo, N.D.; Qi, Y.; Qian, D.; Chou, F.-C.; et al. Topological Type-II Dirac Fermions Approaching the Fermi Level in a Transition Metal Dichalcogenide $NiTe_2$. *Chem. Mater.* **2018**, *30*, 4823–4830. [CrossRef]
12. Sun, Y.; Wu, S.-C.; Ali, M.N.; Felser, C.; Yan, B. Prediction of Weyl Semimetal in Orthorhombic $MoTe_2$. *Phys. Rev. B* **2015**, *92*, 161107. [CrossRef]
13. Deng, K.; Wan, G.; Deng, P.; Zhang, K.; Ding, S.; Wang, E.; Yan, M.; Huang, H.; Zhang, H.; Xu, Z.; et al. Experimental Observation of Topological Fermi Arcs in Type-II Weyl Semimetal $MoTe_2$. *Nat. Phys.* **2016**, *12*, 1105–1110. [CrossRef]
14. Witteveen, C.; Górnicka, K.; Chang, J.; Månsson, M.; Klimczuk, T.; Rohr, F.O. von Polytypism and Superconductivity in the NbS_2 System. *Dalton Trans.* **2021**, *50*, 3216–3223. [CrossRef] [PubMed]
15. Castro Neto, A.H. Charge Density Wave, Superconductivity, and Anomalous Metallic Behavior in 2D Transition Metal Dichalcogenides. *Phys. Rev. Lett.* **2001**, *86*, 4382–4385. [CrossRef] [PubMed]
16. Dutta, U.; Malavi, P.S.; Sahoo, S.; Joseph, B.; Karmakar, S. Pressure-Induced Superconductivity in Semimetallic 1T-$TiTe_2$ and Its Persistence upon Decompression. *Phys. Rev. B* **2018**, *97*, 060503. [CrossRef]
17. Klemm, R.A. Pristine and Intercalated Transition Metal Dichalcogenide Superconductors. *Phys. C* **2015**, *514*, 86–94. [CrossRef]
18. Marseglia, E.A. Transition Metal Dichalcogenides and Their Intercalates. *Int. Rev. Phys. Chem.* **1983**, *3*, 177–216. [CrossRef]
19. Lerf, A. Storylines in Intercalation Chemistry. *Dalton Trans.* **2014**, *43*, 10276–10291. [CrossRef]
20. Parkin, S.S.P.; Friend, R.H. 3d Transition-Metal Intercalates of the Niobium and Tantalum Dichalcogenides. I. Magnetic Properties. *Philos. Mag. B* **1980**, *41*, 65–93. [CrossRef]

21. Inoue, M.; Hughes, H.P.; Yoffe, A.D. The Electronic and Magnetic Properties of the 3d Transition Metal Intercalates of TiS$_2$. *Adv. Phys.* **1989**, *38*, 565–604. [CrossRef]

22. Koyano, M.; Horisaka, S.; Negishi, H.; Sasaki, M.; Inoue, M.; Suzuki, N.; Motizuki, K. Magnetic Scattering of Conduction Carriers in 3d Transition-Metal Intercalates of M$_x$TiS$_2$ (M = Mn, Fe, Co, and Ni). *J. Low Temp. Phys.* **1990**, *78*, 141–154. [CrossRef]

23. Voorhoeve, J.M.; van den Berg, N.; Robbins, M. Intercalation of the Niobium-Diselenide Layer Structure by First-Row Transition Metals. *J. Solid State Chem.* **1970**, *1*, 134–137. [CrossRef]

24. Yacobi, B.G.; Boswell, F.W.; Corbett, J.M. The Fundamental Absorption Edge in Ni$_x$ZrS$_2$. *Mater. Res. Bull.* **1979**, *14*, 1033–1038. [CrossRef]

25. Buhannic, M.; Danot, M. Iron Migration in the Van Der Waals Gap of Zirconium Disulfide: Time Evolution of the Fe$_x$ZrS$_2$ Compounds. *Solid State Commun.* **1990**, *73*, 739–742. [CrossRef]

26. Parkin, S.S.P.; Friend, R.H. 3*d* Transition-Metal Intercalates of the Niobium and Tantalum Dichalcogenides. II. Transport Properties. *Philos. Mag. B* **1980**, *41*, 95–112. [CrossRef]

27. Chen, C.-W.; Chikara, S.; Zapf, V.S.; Morosan, E. Correlations of Crystallographic Defects and Anisotropy with Magnetotransport Properties in Fe$_x$TaS$_2$ Single Crystals $0.23 \leq x \leq 0.35$. *Phys. Rev. B* **2016**, *94*, 054406. [CrossRef]

28. Inoshita, T.; Hirayama, M.; Hamada, N.; Hosono, H.; Murakami, S. Topological Semimetal Phases Manifested in Transition Metal Dichalcogenides Intercalated with 3*d* Metals. *Phys. Rev. B* **2019**, *100*, 121112. [CrossRef]

29. Maniv, E.; Nair, N.L.; Haley, S.C.; Doyle, S.; John, C.; Cabrini, S.; Maniv, A.; Ramakrishna, S.K.; Tang, Y.-L.; Ercius, P.; et al. Antiferromagnetic Switching Driven by the Collective Dynamics of a Coexisting Spin Glass. *Sci. Adv.* **2021**, *7*, eabd8452. [CrossRef]

30. Le Blanc-Soreau, A.; Rouxel, J.; Gardette, M.-F.; Gorochov, O. Proprietes electriques et magnetiques de Mn$_{0,25}$NbS$_2$ et Mn$_{0,33}$NbS$_2$. *Mater. Res. Bull.* **1976**, *11*, 1061–1071. [CrossRef]

31. Yamasaki, Y.; Moriya, R.; Arai, M.; Masubuchi, S.; Pyon, S.; Tamegai, T.; Ueno, K.; Machida, T. Exfoliation and van Der Waals Heterostructure Assembly of Intercalated Ferromagnet Cr$_{1/3}$TaS$_2$. *2D Mater.* **2017**, *4*, 041007. [CrossRef]

32. Arai, M.; Moriya, R.; Yabuki, N.; Masubuchi, S.; Ueno, K.; Machida, T. Construction of van Der Waals Magnetic Tunnel Junction Using Ferromagnetic Layered Dichalcogenide. *Appl. Phys. Lett.* **2015**, *107*, 103107. [CrossRef]

33. Danz, T.; Liu, Q.; Zhu, X.D.; Wang, L.H.; Cheong, S.W.; Radu, I.; Ropers, C.; Tobey, R.I. Structural and Magnetic Characterization of Large Area, Free-Standing Thin Films of Magnetic Ion Intercalated Dichalcogenides Mn$_{0.25}$TaS$_2$ and Fe$_{0.25}$TaS$_2$. *J. Phys. Condens. Matter* **2016**, *28*, 356002. [CrossRef] [PubMed]

34. Ellermeier, J.; Näther, C.; Bensch, W. Tris(Ethylenediamine-N,N′)Nickel(II) Tetrathiomolybdate. *Acta Crystallogr. Sect. C Cryst. Struct. Commun.* **1999**, *55*, 501–503. [CrossRef]

35. Ellermeier, J.; Stähler, R.; Bensch, W. Two New [Ni(Tren)$_2$]$^{2+}$ Complexes: [Ni(Tren)$_2$]Cl$_2$ and [Ni(Tren)$_2$]WS$_4$. *Acta Crystallogr. Sect. C Cryst. Struct. Commun.* **2002**, *58*, m70–m73. [CrossRef]

36. Ellermeier, J.; Bensch, W. Solvothermal Syntheses, Crystal Structures and Properties of Thiomolybdates with Complex Transition Metal Cations. *Z. Naturforsch. B J. Chem. Sci.* **2001**, *56*, 611–619. [CrossRef]

37. Sokolov, M.; Virovets, A.; Nadolinnyi, V.; Hegetschweiler, K.; Fedin, V.; Podberezskaya, N.; Fedorov, V. Nb$_2$S$_2$$^{4+}$ Complexes with 1,1-Dithioacid Ligands. *Inorg. Chem.* **1994**, *33*, 3503–3509. [CrossRef]

38. Sengupta, S.K.; Kumar, S. Thermal Studies on Metal Dithiocarbamato Complexes. A Review. *Thermochim. Acta* **1984**, *72*, 349–361. [CrossRef]

39. Sharma, A.K. Thermal Behaviour of Metal-Dithiocarbamates. *Thermochim. Acta* **1986**, *104*, 339–372. [CrossRef]

40. Poisot, M.; Bensch, W.; Fuentes, S.; Alonso, G. Decomposition of Tetra-Alkylammonium Thiomolybdates Characterised by Thermoanalysis and Mass Spectrometry. *Thermochim. Acta* **2006**, *444*, 35–45. [CrossRef]

41. Poisot, M.; Bensch, W. Decomposition of Tetraalkylammonium Thiotungstates Characterized by Thermoanalysis, Mass Spectrometry, X-Ray Diffractometry and Scanning Electron Microscopy. *Thermochim. Acta* **2007**, *453*, 42–51. [CrossRef]

42. Sokolov, M.N.; Rogachev, A.V.; Abramov, P.A.; Fedin, V.P. Thioxanthate Complexes of {Nb$_2$S$_4$}$^{4+}$. *Polyhedron* **2015**, *85*, 727–731. [CrossRef]

43. Raston, C.L.; White, A.H.; Willis, A.C. Crystal Structure of Tris(Dithiocarbamato)Cobalt(III). *J. Chem. Soc. Dalton Trans.* **1975**, 2429–2432. [CrossRef]

44. Gasparri, G.F.; Nardelli, M.; Villa, A. The Crystal and Molecular Structure of Nickel Bis(Dithiocarbamate). *Acta Cryst.* **1967**, *23*, 384–391. [CrossRef]

45. Nakamoto, K.; Fujita, J.; Condrate, R.A.; Morimoto, Y. Infrared Spectra of Metal Chelate Compounds. IX. A Normal Coordinate Analysis of Dithiocarbamato Complexes. *J. Chem. Phys.* **1963**, *39*, 423–427. [CrossRef]

46. Rijnsdorp, J.; Haas, C. Fine Structure in the Absorption Edge Spectrum of NbS$_2$Y$_2$ (Y = Cl, Br, I). *J. Phys. Chem. Solids* **1980**, *41*, 375–384. [CrossRef]

47. Kato, K.; Tamura, S. Die Kristallstruktur von T-Nb$_2$O$_5$. *Acta Crystallogr. Sect. B Struct. Crystallogr. Cryst. Chem.* **1975**, *31*, 673–677. [CrossRef]

48. Jellinek, F.; Brauer, G.; Müller, H. Molybdenum and Niobium Sulphides. *Nature* **1960**, *185*, 376–377. [CrossRef]

49. Katzke, H. Stacking Disorder in 2H-NbS$_2$ and Its Intercalation Compounds K$_x$(H$_2$O)$_y$NbS$_2$ I. Description and Model Calculations of Stacking Faults in the Host Lattice NbS$_2$. *Z. Kristallogr. Cryst. Mater.* **2009**, *217*, 127–130. [CrossRef]

50. Fisher, W.G.; Sienko, M.J. Stoichiometry, Structure, and Physical Properties of Niobium Disulfide. *Inorg. Chem.* **1980**, *19*, 39–43. [CrossRef]

51. Huang, C.; Wang, X.; Wang, D.; Zhao, W.; Bu, K.; Xu, J.; Huang, X.; Bi, Q.; Huang, J.; Huang, F. Atomic Pillar Effect in Pd_xNbS_2 To Boost Basal Plane Activity for Stable Hydrogen Evolution. *Chem. Mater.* **2019**, *31*, 4726–4731. [CrossRef]

52. Wiegers, G.A.; Haange, R.J.; van Bolhuis, F. The Crystal Structure of Stage-2 $4H-Ag_{0.22}NbS_2$. *Phys. Status Solidi A* **1988**, *107*, 817–824. [CrossRef]

53. Van der Lee, A.; van Smaalen, S.; Wiegers, G.A.; de Boer, J.L. Order-Disorder Transition in Silver-Intercalated Niobium Disulfide Compounds. I. Structural Determination of $Ag_{0.6}NbS_2$. *Phys. Rev. B* **1991**, *43*, 9420–9430. [CrossRef] [PubMed]

54. Mangelsen, S.; Srinivasan, B.R.; Schürmann, U.; Kienle, L.; Näther, C.; Bensch, W. Nanostructured Tungsten Sulfides: Insights into Precursor Decomposition and the Microstructure Using X-Ray Scattering Methods. *Dalton Trans.* **2019**, *48*, 1184–1201. [CrossRef] [PubMed]

55. Van den Berg, J.M.; Cossee, P. Structural Aspects and Magnetic Behaviour of NbS_2 and TaS_2 Containing Extra Metal Atoms of the First Transition Series. *Inorg. Chim. Acta* **1968**, *2*, 143–148. [CrossRef]

56. Rijnsdorp, J.; de Lange, G.J.; Wiegers, G.A. Preparation, Structures, and Properties of Niobium Chalcogenide Halides, NbX_2Y_2 (X = S, Se; Y = Cl, Br, I). *J. Solid State Chem.* **1979**, *30*, 365–373. [CrossRef]

57. Teske, C.L.; Bensch, W. On Crystal Structure Investigations of α- and β-Ammoniumdithiocarbamate $NH_4CS_2NH_2$ and the Role of Hydrogen Bonding. *Z. Anorg. Allg. Chem.* **2010**, *636*, 356–362. [CrossRef]

58. Schäfer, H.; Beckmann, W. Beiträge Zur Chemie der Elemente Niob und Tantal. LIV. Sulfid- und Selenidhalogenide des Niobs. *Z. Anorg. Allg. Chem.* **1966**, *347*, 225–230. [CrossRef]

59. Schnering, H.G.v.; Beckmann, W. Beiträge zur Chemie der Elemente Niob und Tantal. LV. Die Kristallstruktur von NbS_2Cl_2. *Z. Anorg. Allg. Chem.* **1966**, *347*, 231–239. [CrossRef]

60. Coelho, A.A. TOPAS and TOPAS-Academic: An Optimization Program Integrating Computer Algebra and Crystallographic Objects Written in C^{++}. *J. Appl. Cryst.* **2018**, *51*, 210–218. [CrossRef]

61. Coelho, A.A. Indexing of Powder Diffraction Patterns by Iterative Use of Singular Value Decomposition. *J. Appl. Cryst.* **2003**, *36*, 86–95. [CrossRef]

62. Coelho, A.A. Whole-Profile Structure Solution from Powder Diffraction Data Using Simulated Annealing. *J. Appl. Cryst.* **2000**, *33*, 899–908. [CrossRef]

63. *CrysAlis PRO*, version 171.43, Program Package for Crystal Structure Determinations; Rigaku: Wroclow, Poland, 2020.

64. *X-Area*, Version 1.44, Program Package for Crystal Structure Determinations; STOE & Cie GmbH: Darmstadt, Germany, 2002.

65. Sheldrick, G.M. SHELXT—Integrated Space-Group and Crystal-Structure Determination. *Acta Crystallogr. Sect. A Found. Adv.* **2015**, *71*, 3–8. [CrossRef] [PubMed]

66. Sheldrick, G.M. Crystal Structure Refinement with SHELXL. *Acta Crystallogr. Sect. C Struct. Chem.* **2015**, *71*, 3–8. [CrossRef]